On Rigorous Model-Order Reduction of the Thermal and Oxygen Storage Dynamics of Three Way Catalytic Converters

Federico Dettu
Energy Resources Engineering Department,
Stanford University,
Stanford, CA 94305
e-mail: fdettu@stanford.edu

Simona Onori
Energy Resources Engineering Department,
Stanford University,
Stanford, CA 94305
e-mail: sonori@stanford.edu

We present a reduced-order model (ROM) for the temperature and oxygen storage dynamics of three way catalysts (TWCs). The thermal and oxygen storage dynamics are described using a set of coupled, nonlinear partial differential equations (PDEs) developed and experimentally validated in previous research. Advancements in on-board diagnostic (OBD) design are moving in the direction of using physics-based models that would retain as much physical insights as possible. Retaining the one-dimensional (1D) evolution of the internal storage dynamics along the device length is key for the development of accurate emission control strategies. In this work, we adopt the numerical projection orthogonal approach combined with the analytical features of Galerkin reduction method to define a set of ordinary differential equations (ODEs) to describe the oxygen storage and temperature dynamics throughout the device life. Using experimental data collected over three TWC devices, each of different age, and under the excitation of different real drive cycles, we validate the model and quantify the relation between the number of reduced-order states versus model accuracy for devices both new and at different stages of life. The input dependent characteristics of the developed reduced-model model is also investigated using a power spectral density (PSD) analysis. Finally, we show that an initial tuning of the reduced model parameters for a fresh catalyst guarantees satisfactory modeling performance throughout the device life, regardless of the driving scenario.
[DOI: 10.1115/1.4048359]

1 Introduction

Over the years, the need for more stringent emission regulations has led to significant technological advancements in the automotive industry [1]. While electric vehicles sales are growing every year, consequently to the lowering price of lithium-ion batteries, conventional, and hybrid vehicles still represent the biggest market share. This is expected to continue for the next couple of decades, with conventional, and hybrid vehicles sales accounting for more then 50% of the total light-duty vehicles sales by 2040 (see Ref. [2]). All those vehicles will necessitate the implementation of an advanced after-treatment system to meet the ever stricter emission regulation targets [3]. In order to meet the strict emission standards [4], mostly regarding harmful gases such as carbon monoxide (CO), nitrogen oxides (NO_x), and hydrocarbons (HC), advances have been made toward developing sophisticated engine and after-treatment systems.

Automotive manufacturers have moved their interests toward gasoline direct injection (GDI) technology, that gives better fuel economy and power out [5] than port fuel injection engines at the cost of higher particulate output [6]. As the complexity in the design of automotive engines has increased, GDI engine manufacturers have been challenged to develop efficient after-treatment and software systems to monitor the operating conditions of various components. One such development includes the thermal oxidation of carbon monoxide and hydrocarbons, whereby air is pumped into the exhaust system to allow for a complete combustion of all gases [7]. Another technique used to improve the after-treatment system efficiency is the exhaust gas recirculation (EGR) technology in which the reduction of nitrogen oxides is aided by re-introducing some of the exhaust gas back into the engine, and

mixing it with the fresh air–fuel mixture. This acts as a diluent in the mixture, lowering the heat release and reducing the peak in-cylinder temperature, thus reducing the rate of formation of the dangerous NO_x [8]. The most widely used emission mitigation strategies involve the use of catalytic converters and gas particulate filters to reduce the emission of harmful gases and particulate matter [9].

As stated in Ref. [10], the principle under which the internal combustion engine operates is that the fuel needs to be oxidized in order to create the pressure to drive the pistons. This pressure is generated from the heat which is released after the chemical reaction between the fuel and air. In an ideal combustion reaction, oxygen (O_2) reacts with the hydrocarbons (HC) to produce carbon dioxide (CO_2), water (H_2O), and heat. However, the intake air is not pure oxygen, as it contains nitrogen (N_2). This might lead to the formation of oxides of nitrogen (NO_x). In ideal conditions (complete combustion) the nitrogen should be a bypass product of the combustion reaction, in reality the latter reacts with oxygen in different ways leading to the formation of NO_x. Moreover, when the carbon is not completely oxidized in the reaction, it might generate CO (and soot). Similarly, an incomplete combustion of the fuel might lead to presence of unburned hydrocarbons in the exhaust gas.

In a three way catalyst (TWC), the redox (reduction-oxidation) reactions convert harmful pollutants to less toxic emissions. It is called a "three way" catalyst since it aids in the reduction of nitrogen oxides to less harmful nitrogen gas (N_2), oxidation of carbon monoxide (CO) to carbon dioxide (CO_2), and oxidation of unburnt hydrocarbons (HC) to carbon dioxide (CO_2), and water (H_2O). These chemical reactions occur simultaneously inside the catalyst and the efficiency with which the redox reactions occur depends highly on the air–fuel ratio (AFR) and the temperature inside the catalyst. The AFR is the ratio of the mass of air to fuel in the mixture inside the internal combustion engine during ignition, and it is more often expressed using its normalized measure, λ, which is

the ratio between the actual AFR and the AFR at stoichiometric conditions (the exact air–fuel ratio needed to produce chemically complete combustion). The AFR and λ are computed as follows:

$$\lambda = \frac{AFR_{(actual)}}{AFR_{(stoichiometric)}} = \frac{m_{air}/m_{fuel}}{AFR_{(stoichiometric)}} \quad (1)$$

where

$$\begin{aligned} m_{air} &= \text{mass of air} \\ m_{fuel} &= \text{mass of fuel} \end{aligned} \quad (2)$$

The stoichiometric AFR for a gasoline engine is [11]

$$AFR_{(stoichiometric)} = 14.7 \quad (3)$$

If the AFR is within a narrow region around the stoichiometric value the efficiency of the device is close to 1, i.e., the success of complete reduction and oxidation reactions is higher. The efficiency decreases when the AFR falls outside this range. When the AFR is lower than the stoichiometric value, the combustion occurs in rich conditions ($\lambda < 1$). In this case, the oxygen is utilized during fuel combustion and there is not sufficient amount left to carry out the oxidation reactions inside the catalyst. When the AFR is greater than the stoichiometric value, the engine operates under lean condition ($\lambda > 1$), i.e., there is excess oxygen available inside the catalyst and hence the reduction reaction does not occur completely.

The catalytic conversion efficiency also depends on the temperature inside the TWC. The chemical conversions take place with an efficiency greater than the 50% when the temperature is greater than the light-off temperature [12], which is in general different for different catalysts. Therefore, the catalyst temperature dynamics plays an important role in the control of harmful emissions, and the ability to monitor and predict the catalyst temperature will help design an efficient exhaust system. Since there are no sensors that can be used to measure this quantity in real-time in commercial vehicles, being able to accurately estimate it is crucial for on-board diagnostics (OBD) design.

Common methods to model the TWC dynamics rely on two types of approaches, physics-based, and empirical-based models, respectively.

Physics-based models lead to a description of the system in the form of partial differential equations (PDEs), starting from first principles [13–17]. These works rely on energy and mass conservation, and kinetic dynamics modeling, to obtain high accuracy in the prediction of the undesired engine emission species within the catalyst. These models are computationally intensive and require the knowledge of the species concentration at the catalyst inlet, which are nonavailable in production vehicles, and they are mostly used as a tool for system design and analysis. As a result, their real-time implementation for OBD purposes is not feasible. Modeling the TWC as a one-dimensional (1D) adiabatic channel where the internal dynamics are obtained from the mass transport and the gas and solid energy balances between the gas phase and the washcoat has shown to be a good compromise between accuracy and real-time computational needs [18–22]. In Ref. [18], a 1D control-oriented model for the temperature and oxygen storage dynamics of the TWC is derived starting from first principle equations, and a semi-empirical approach is used to model the heat generation resulting from the chemical conversion reactions and a reduced number of chemical species is considered. The concentrations of each species are lumped together, in that not distinction is made between the concentration in the gas phase and in the solid one. Similar assumptions are made in Refs. [19] and [22], while in the latter the concentration of H_2 is considered too, thus yielding a more complex and accurate model.

In Ref. [20], the authors discretize the comprehensive physics-based model presented in Ref. [17] along the axial direction of the TWC, in order to obtain a model suitable for real-time estimation via an extended Kalman filter. Empirical models make use of maps and transfer functions and other approximations to model TWC dynamics, therefore, a device-specific calibration is required before their implementation. For instance, in Ref. [12], the authors propose a model based on two different transfer functions for the oxygen storage, and simplify the thermal dynamics through a nonlinear function. In Ref. [23], a control-oriented model based on different nonlinear functions is proposed, each one for a different operating region. However, the spatial and temperature dependence of the oxygen storage level are neglected, since the only model input considered is the AFR. Similarly, the temperature dependence is also neglected in Ref. [24]. Moreover, map-based models do not allow for the formulation of a state observer, which is often needed in real-time scenarios, when the measurements are affected by noise, and the parameters can change, for example, due to the TWC aging.

A further step in the development of model-based OBD routines is from the adoption of reduced-order techniques that would allow to create a control-oriented model from a physics-based one [25–27].

In Ref. [28], the authors developed a reduced model starting from Ref. [18] for the catalyst thermal dynamics, using a Galerkin-proper orthogonal decomposition (POD) approach. Similarly, in Ref. [29], a Galerkin-POD approach on the same thermal model is proposed along with an artificial neural network model to approximate the nonlinear reaction heat generation dynamics. Both models do not consider the oxygen storage dynamics, which, on the other hand, is key for the development of an air–fuel ratio control strategy for emission mitigation.

This paper synthesizes a reduced-order control-oriented model which accounts for the thermal and oxygen storage dynamics of a TWC. The reduced model is developed starting from a set of nonlinear coupled PDEs describing the device internal dynamics along the longitudinal direction. With respect to the PDE model presented in Ref. [18], the thermal model does not neglect the dynamics of the gas phase and the spatial derivatives in the PDEs. An identification procedure is performed by means of the particle swarm optimization (PSO) algorithm to find the parameters of the thermal model using real data obtained from differently aged TWCs. The physics-based model is then reduced via the Galerkin projection method, a formal mathematical method which can be used to transform a set of PDEs into a set of ordinary differential equations (ODEs), thus removing the space-dependence from the equations and make it prone for estimation design. The reduced dynamics are approximated using a set of orthogonal basis functions. The latter are chosen to be analytic harmonic functions for the thermal model, while they are numerically obtained through the POD algorithm for the oxygen storage model. The reduced system parameters are fully determined once the number of basis functions is selected. The Galerkin method allows to easily select the model complexity by changing the number of basis functions. As this number increases, the model prediction performance improves, while more computational power is required. It is then possible to adapt the model to the computational power of the electronic control units (ECU), which can eventually improve over the years, and obtain more accurate models. Moreover, the reduced model is tested against data coming from differently aged catalysts (three aged TWCs are considered), showing its effectiveness. To the best of our knowledge, a rigorous TWC control-oriented model design using formal reduction methods applied to an experimentally validated physics-based and age-dependent model had not been investigated.

This paper is structured as follows. In Sec. 2 the physics-based model is presented. In Sec. 3 the parameters identification for the proposed thermal model is shown. Then, in Secs. 4 and 5, respectively, the reduced-order model (ROM) derivation is showed in details, and its performance is compared to that of the PDE model, for different driving cycles and catalyst aging processes. Finally, final remarks are outlined in Sec. 6.

2 Three Way Catalyst Model

The TWC model used in this work consists of the thermal and oxygen storage dynamics. The dynamics are expressed as a set of PDEs which are coupled and nonlinear in nature. The thermal model describes the temperature profile of the exhaust gas and the catalyst substrate, whereas the oxygen storage model predicts the TWC oxygen storage level. The variations of those quantities are described in time and space, along the flow direction. (A schematic of the TWC is depicted in Fig. 1, where $L = 0.068$ m is the length of the device used in this study and $z \in [0,L]$ is the spatial coordinate along which the dynamics are considered with Δz the step used for the longitudinal discretization. The model inputs are the exhaust mass-flowrate $\dot{m}_{exh}(t)$, the temperature $T_{exh}(t)$, and the normalized air–fuel ratio at the inlet $\lambda_{pre}(t)$. Those inputs are available to the ECU. In particular, λ_{pre} is from an Universal Exhaust-Gas Oxygen (UEGO) sensor, while $\dot{m}_{exh}$ is estimated internally by the ECU. The model states are the gas temperature $T_g(z,t)$, the catalyst temperature $T_{cat}(z,t)$ and the species concentration $[X](z,t)$, where $[X] = [O_2], [CO], [CO_2], [Ce_2O_4]$. Finally, the model outputs are the TWC gas phase temperature at the outlet $T_{g,out}(t) = T_g(L,t)$ and the normalized air–fuel ratio at the outlet (see Fig. 2) $\lambda_{out}(t)$. The latter is defined as [30]

$$\lambda_{out} = \frac{2[O_2](L,t) + [CO](L,t) + 2[CO_2](l,t)}{2[CO](l,t) + 2[CO_2](l,t)} \quad (4)$$

The normalized AFR at the outlet is measured via an UEGO sensor, and the catalyst temperature, $T_{cat,mid}$, is measured via the insertion of a thermocouple in the center location of the device [31]. These signals are used for model validation.

2.1 Thermal Dynamics.
The thermal dynamics of the TWC is defined by the following system of PDE coupled equations

$$\rho_g \varepsilon c_{p,g} \frac{\partial T_g}{\partial t} = \varepsilon \lambda_g \frac{\partial^2 T_g}{\partial z^2} - \frac{\dot{m}_{exh}}{A_{cs}} c_{p,g} \frac{\partial T_g}{\partial z}$$
$$+ hA_{geo}(T_{cat} - T_g)$$
$$\rho_s (1-\varepsilon) c_{p,s} \frac{\partial T_{cat}}{\partial t} = (1-\varepsilon)\lambda_s \frac{\partial^2 T_{cat}}{\partial z^2} -$$
$$- hA_{geo}(T_{cat} - T_g) + K_{reac}\dot{m}_{exh} \quad (5)$$
$$T_g(z,0) = T_{cat}(z,0) = T_{exh}(0)$$
$$T_g(0,t) = T_{exh}(t), \quad \left.\frac{\partial T_g}{\partial z}\right|_{z=L} = 0$$
$$\left.\frac{\partial T_{cat}}{\partial z}\right|_{z=0} = \left.\frac{\partial T_{cat}}{\partial z}\right|_{z=L} = 0$$

The physical meaning of the symbols in Eq. (5) is explained in the Nomenclature table. It is assumed that the substrate temperature is always greater than the catalyst light-off temperature, $T_{cat} > T_{light-off}$. This implies that the heat generated from the reactions ins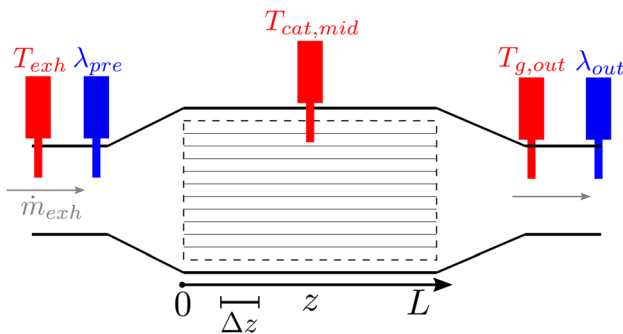ide the TWC can be approximated as a linear function of the mass flow rate of the exhaust gas, as showed in Ref. [31]. However, this approximation is accurate only as long as the catalyst operates around stoichiometric conditions, where the hydrocarbons and the CO are almost completely reduced. This is usually a valid assumption as the after-treatment control algorithms are tuned to maintain the stoichiometry operation. For the purpose of model-order reduction development, and with the idea in mind to have the least approximated physics-based model to start with, to the equations used in Ref. [31], we added the gas temperature storage term $\rho_g \varepsilon c_{p,g}(\partial T_g/\partial t)$, the conduction along the substrate $(1-\varepsilon)(\partial^2 T_{cat}/\partial z^2)$ and the conduction in the gas phase $\varepsilon \lambda_g(\partial T_g/\partial z^2)$ terms. For simplicity of notation, we rewrite the thermal dynamics (5) as

$$\frac{\partial T_g}{\partial t} = \mathcal{D}_1 \frac{\partial^2 T_g}{\partial z^2} - \mathcal{D}_2 \dot{m}_{exh} \frac{\partial T_g}{\partial z} + \mathcal{D}_3(T_{cat} - T_g)$$
$$\frac{\partial T_{cat}}{\partial t} = \mathcal{D}_4 \frac{\partial^2 T_{cat}}{\partial z^2} + \mathcal{D}_5 \dot{m}_{exh} - \mathcal{D}_6(T_{cat} - T_g) \quad (6)$$

where the parameters $\mathcal{D}_1, \mathcal{D}_2, \ldots, \mathcal{D}_6$ are defined as follows:

$$\mathcal{D}_1 = \frac{\lambda_g}{\rho_g c_{p,g}}, \quad \mathcal{D}_2 = \frac{1}{\rho_g \varepsilon A_{cs}}$$
$$\mathcal{D}_3 = \frac{hA_{geo}}{\rho_g \varepsilon c_{p,g}}, \quad \mathcal{D}_4 = \frac{\lambda_s}{\rho_s c_{p,s}} \quad (7)$$
$$\mathcal{D}_5 = \frac{hA_{geo}}{\rho_s (1-\varepsilon) c_{p,s}}, \quad \mathcal{D}_6 = \frac{K_{reac}}{\rho_s (1-\varepsilon) c_{p,s}}$$

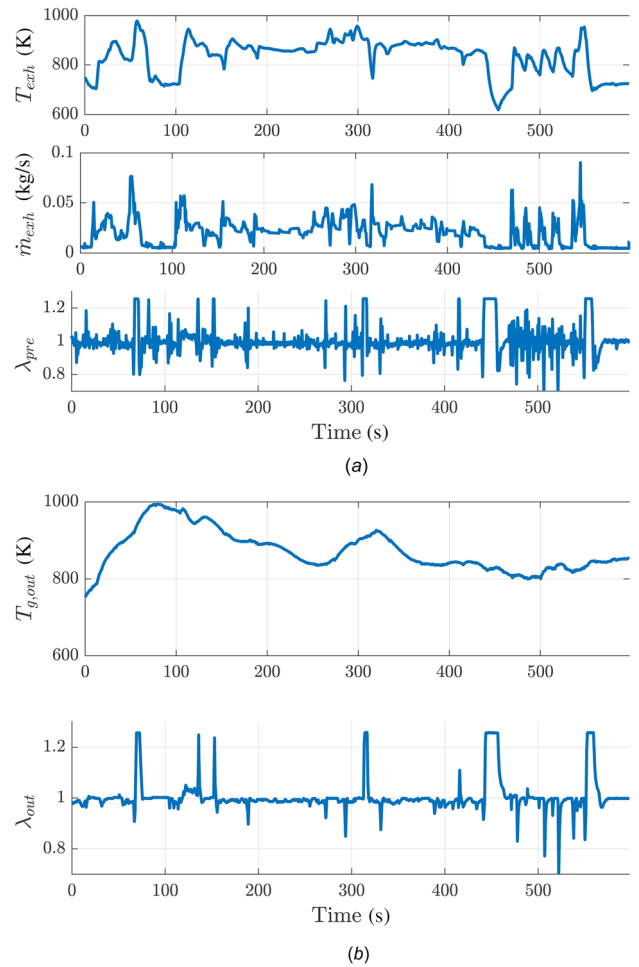Fig. 1 Schematic of the TWC considered in this work showing the input and output sensor positions
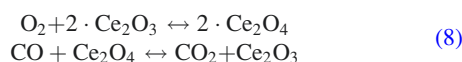

Fig. 2 Example of the available inputs and outputs taken from driving a FUDS driving cycle: (a) measured model inputs and (b) measured model outputs

For the numerical solution of the PDE thermal model, the *pdepe* MATLAB function has been used [32]. The algorithm implemented with this function discretizes the PDEs in space, and then integrates them in time using the *ode15s* MATLAB function. A maximum step size of $0.1 \cdot |t_f - t_0|$ is used in the integration, whereas t_0 and t_f are the first and the last time instants of the simulation. The spatial discretization is performed using the discretization step $\Delta z_{\text{therm}} = (L/Z_{\text{therm}})$ given by dividing the catalyst length L by Z_{therm} cells of the same length.

2.2 Oxygen Storage Dynamics. The model derived from Ref. [18] is briefly described in this section. The simplified model (in the sense that only two chemical reactions are considered, with a reduced number of species) of the oxygen storage is given by two reverse heterogeneous reactions

$$
\begin{aligned}
O_2 + 2 \cdot Ce_2O_3 &\leftrightarrow 2 \cdot Ce_2O_4 \\
CO + Ce_2O_4 &\leftrightarrow CO_2 + Ce_2O_3
\end{aligned}
\tag{8}
$$

where species O_2, CO, CO_2 correspond to the gas phase and species Ce_2O_3 and Ce_2O_4 to the solid phase. The reaction rates R_1 and R_2 of the forward and backward reactions are defined as follows:

$$
\begin{aligned}
R_1 &= k_1^f \cdot (\text{OSC} - [Ce_2O_4])^2 \cdot [O_2] - k_1^b \cdot [Ce_2O_4]^2 \cdot c_0 \\
R_2 &= k_2^f \cdot [Ce_2O_4] \cdot [CO] - k_2^b \cdot (\text{OSC} - [Ce_2O_4]) \cdot [CO_2]
\end{aligned}
\tag{9}
$$

where $c_0 = (P/RT_g)$ is the total exhaust gas concentration defined by the ideal gas law, and k_1^f, k_1^b, k_2^f, k_2^b are the forward and backward reaction coefficients for the two reactions, according to the Arrhenius's type equations

$$
\begin{aligned}
k_1^f &= A_1 e^{-\frac{E_1}{RT_{\text{cat}}}}, \quad k_1^b = A_1 e^{-\frac{E_1 + \Delta G_1}{RT_{\text{cat}}}} \\
k_2^f &= A_2 e^{-\frac{E_2}{RT_{\text{cat}}}}, \quad k_2^b = A_2 e^{-\frac{E_2 + \Delta G_2}{RT_{\text{cat}}}}
\end{aligned}
\tag{10}
$$

where E_1, E_2 are the activation energies, A_1, A_2 are the reaction rate constants and ΔG_1, ΔG_2 are the Gibbs energy change. Moreover, in the backward reaction coefficients, according to [17]

$$
\begin{aligned}
\frac{\Delta G_1}{RT_{\text{cat}}} &\approx \frac{2(a_{Ce_2O_4} + b_{Ce_2O_4})}{T_{\text{cat}} + c_{Ce_2O_4}} - \frac{a_{O_2} T_{cat} + b_{O_2}}{T_{\text{cat}} + c_{O_2}} \\
\frac{\Delta G_2}{RT_{\text{cat}}} &\approx \frac{a_{Ce_2O_4} + b_{Ce_2O_4}}{T_{\text{cat}} + c_{Ce_2O_4}} - \frac{a_{CO_2} T_{cat} + b_{CO_2}}{T_{\text{cat}} + c_{CO_2}} + \frac{a_{CO} T_{cat} + b_{CO}}{T_{\text{cat}} + c_{CO}}
\end{aligned}
\tag{11}
$$

where the parameters a_X, b_X, c_X (where the subscript X indicates the chemical species involved in the reaction) can be identified experimentally.

The concentration balance in the gas phase and in the washcoat are lumped, and for the gas species we write the balance as an advection–reaction equation, with the neglection of the storage term, since the exhaust gas dynamics are much faster than the oxygen storage dynamics (see Ref. [13]). From Ref. [18], the oxidized and empty surface sites ($[Ce_2O_4]$ and $[Ce_2O_3]$) are governed by the following relation, where OSC is constant

$$
[Ce_2O_3](z, t) = \text{OSC} - [Ce_2O_4](z, t)
\tag{12}
$$

Overall, the oxygen storage model reads

$$
\begin{aligned}
0 &= -u \frac{\partial [O_2]}{\partial z} - R_1 \\
0 &= -u \frac{\partial [CO]}{\partial z} - R_2 \\
0 &= -u \frac{\partial [CO_2]}{\partial z} + R_2 \\
\frac{\partial [Ce_2O_4]}{\partial t} &= 2R_1 - R_2
\end{aligned}
\tag{13}
$$

where the spatial velocity u can be written as a function of the exhaust gas mass flowrate, $u = \dot{m}_{\text{exh}}/(c_0 M_{\text{exh}} A_{cs})$, with M_{exh} being the average molar mass of the exaust gas and A_{cs} the TWC cross-sectional area. Additionally, the normalized oxygen storage level ϕ is defined as $[Ce_2O_4]$ normalized by OSC, whose variation with respect to time is given by

$$
\frac{d\phi}{dt} = \frac{1}{\text{OSC}} (2R_1 - R_2)
\tag{14}
$$

Boundary and initial conditions are defined in Eq. (15) and can be obtained from λ_{pre}, for instance, following the procedure showed in Ref. [33]

$$
\begin{aligned}
[O_2](z, 0) &= [O_2](0, t) = [O_2]_{\text{pre}}(t) \\
[CO](z, 0) &= [CO](0, t) = [CO]_{\text{pre}}(t) \\
[CO_2](z, 0) &= [CO_2](0, t) = [CO_2]_{\text{pre}}(t) \\
\frac{\partial [CO]}{\partial z}\bigg|_{z=L} &= \frac{\partial [O_2]}{\partial z}\bigg|_{z=L} = \frac{\partial [CO_2]}{\partial z}\bigg|_{z=L} = 0 \\
[Ce_2O_4](z, 0) &= \frac{\text{OSC}}{2}, \quad \frac{\partial [Ce_2O_4]}{\partial z}\bigg|_{z=0,L} = 0
\end{aligned}
\tag{15}
$$

In Eq. (15), $[X]_{\text{pre}}$ is the concentration for a specie $[X]$ at the TWC inlet. Following the procedure adopted in Ref. [18], the PDE model is discretized using a finite difference upwind scheme. Z_{stor} is the number of discretization cells, and the spatial resolution is obtained as the catalyst length divided by the number of the cells, namely, $\Delta z_{\text{stor}} = L/Z_{\text{stor}}$. The set of discretized PDEs is written in Eq. (16), where the conditions for the first cell have been defined in Eq. (15), and l refers to the lth discretization cell. One should note that, even if the first three equations were partial differential algebraic equations (DAE) in Eq. (13), the concentration of the species $[O_2]$, $[CO]$, $[CO_2]$ is obtained at each time-step through simple algebraic computations, once $[Ce_2O_4]$ is known, without the need for a DAE solver

Table 2 Crosses indicate the availability of the experimental data for the driving cycle and TWC age combination

AGE	FTP	FUDS	US06	FHDS
Green	X	X	X	
Midlife	X	X		
OBD	X			X

Table 3 Identified parameters for the combined FTP and FUDS driving cycles and the different TWCs, by means of the PSO algorithm

Parameter	Green	Midlife	OBD
$\mathcal{D}_1$	4.391×10^{-4}	4.034×10^{-4}	0.0011
$\mathcal{D}_2$	7.844×10^{3}	1.425×10^{4}	1.984×10^{3}
$\mathcal{D}_3$	1.431×10^{5}	3.234×10^{4}	4.100×10^{4}
$\mathcal{D}_4$	6.117×10^{-6}	4.238×10^{-6}	1.6667×10^{-6}
$\mathcal{D}_5$	179.074	134.171	80.750
$\mathcal{D}_6$	2.283	0.444	1.773

Table 1 Summary of the aged catalysts used in this work

	Aging process (equivalent mileage)
Green	Fresh catalyst (0 miles)
Midlife	Engine dyno (50 k miles)
OBD	OBD aged (>150 k miles)

$$[O_2]^l = \frac{[O_2]^{l-1} + k_1^b \left([Ce_2O_4]^l \right)^2 \cdot \frac{c_0 \Delta z_{stor}}{u}}{1 + k_1^f \cdot \frac{\Delta z_{stor}}{u} \left(OSC - [Ce_2O_4]^l \right)^2}$$

$$[CO]^l = \frac{[CO]^{l-1} \left(1 + k_2^b \frac{\Delta z_{stor}}{u} \left(OSC - [Ce_2O_4]^l \right) \right) + k_2^b \frac{\Delta z_{stor}}{u} [CO_2]^{l-1} \left(OSC - [Ce_2O_4]^l \right)}{k_2^b \frac{\Delta z_{stor}}{u} \left(OSC - [Ce_2O_4]^l \right) + k_2^f \frac{\Delta z_{stor}}{u} + 1}$$

$$[CO_2]^l = \frac{[CO_2]^{l-1} \left(1 + k_2^f \frac{\Delta z_{stor}}{u} [Ce_2O_4]^l \right) + k_2^f \frac{\Delta z_{stor}}{u} [CO]^{l-1} [Ce_2O_4]^l}{k_2^b \frac{\Delta z_{stor}}{u} \left(OSC - [Ce_2O_4]^l \right) + k_2^f \frac{\Delta z_{stor}}{u} [Ce_2O_4]^l + 1} \qquad \frac{d[Ce_2O_4]^l}{dt} = 2R_1^l - R_2^l$$

(16)

3 Parameters Identification

Since the storage model was borrowed from previous research [18], we adopted the same parameters values whereas for the thermal dynamics, we run a new identification [31]. The unknown parameters are identified by comparing the thermal model prediction to the available experimental data over TWCs of various ages. Three different catalysts were used: a Green catalyst, a Mid-Life catalyst, and an OBD aged catalyst. The catalysts aging processes are summarized in Table 1. The experimental data were collected for various types of aged TWCs using different driving cycles, according to Table 2. For each driving cycle and TWC type, the experimental data include the mass flow rate $\dot{m}_{exh}(t)$, the exhaust gas temperature upstream of the TWC brick, $T_{exh}(t)$, and the temperature at the center of the TWC brick, $T_{cat,mid}(t)$. The signals are sampled with a sampling frequency of $f_s = 200\,Hz$. From now on, the index k will refer to a time-sampled signal: for instance, the time sampled inlet mass flow rate, at a given time instant $t = k \cdot f_s$ is written as $\dot{m}_{exh}(k \cdot f_s)$. The problem characterized by six parameters to be identified, namely, $\theta_{therm} = [\mathcal{D}_1, \mathcal{D}_2, \mathcal{D}_3, \mathcal{D}_4, \mathcal{D}_5, \mathcal{D}_6]$ has been tackled using the PSO algorithm [34] with the MATLAB function *particleswarm* [35]. The thermal model has been discretized using 20 cells for the identification procedure. The cost function for the identification is defined as the root-mean-square error (RMSE) between $T_{cat,mid}$ and the predicted temperature from the PDE model, $T_{cat,mid}^{pde}$

$$J_{therm} = \sqrt{\sum_{k=1}^{N_s} \frac{\left(T_{cat,mid}(k) - T_{cat,mid}^{pde}(k, \theta_{therm}) \right)^2}{N_s}} \qquad (17)$$

where N_s is the number of time samples in the experiment, and the index k represents the sampled time instant for a time-dependent signal.

The parameters identified with PSO for the three differently aged TWCs are reported in Table 3. For the Green and Midlife catalysts, a combination of the FTP and the FUDS cycles have been used, while for the OBD catalyst, FTP combined with FHDS was used. The catalyst physical parameters can change under aging, especially if high temperatures occur during the process for long period of time (thermal aging) [36]. For the storage model, the identification procedure is not repeated in this study. An example of the PDE model performance (both thermal and storage) is shown in Fig. 3.

The list of the parameters that had been calibrated in the previous research is [18]

$$\theta_{stor} = [A_1 \, A_2 \, E_1 \, E_2 \, a_{Ce_2O_4} \, b_{Ce_2O_4} \, OSC] \qquad (18)$$

4 Model-Order Reduction

In the following, the procedure for the reduction of the PDE based model is shown. Two different approaches have been used for the thermal and oxygen storage models, and they are described in details in the following.

4.1 Reduction of the Thermal Dynamics. The reduction of the thermal dynamics is performed using a Galerkin projection algorithm. The algorithm takes the PDE model as an input, and generates an ODE model, thus eliminating the spatial dependence of the dynamics. The obtained model has the same inputs of the original model. The first step of this procedure is the identification of a trial solution for the model states, which results in having each state decomposed as the finite sum of $N+1$ time-varying coefficients multiplied by spatially varying orthogonal basis functions. However, since the left boundary condition (BC) for T_g is time-varying and defined by $T_{exh}(t)$, a change of state variable has
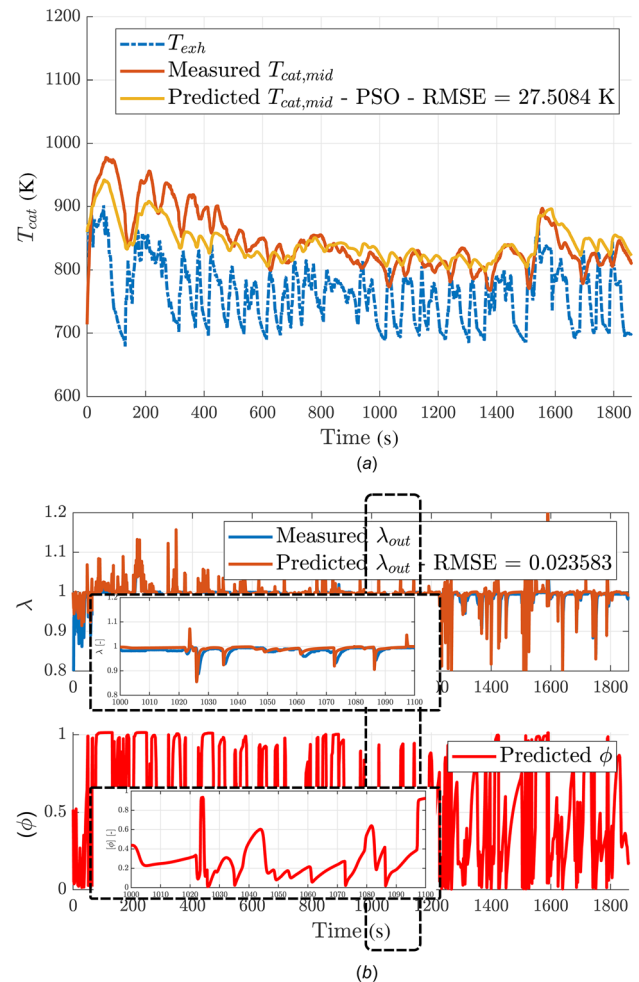

Fig. 3 Model prediction performance for the Green TWC over the FTP driving cycle: (*a*) measured versus predicted $T_{cat,mid}$ and (*b*) measured versus predicted λ_{out} (upper plot) and predicted ϕ (lower plot)

to be performed in order to apply the Galerkin method. In fact, typical orthogonal functions are usually time independent, and without this preliminary step, a reduced model satisfying the boundary conditions cannot be obtained. We define the following change of variables:

$$T_g(z,t) = \hat{T}_g(z,t) + f(z) \cdot T_{\text{exh}}(t) \qquad (19)$$

where $f(z) = 1 - \sin(\pi z/2L)$. One can easily verify that the BCs for the new state $\hat{T}_g(z,t)$ are

$$\hat{T}_g(0,t) = 0, \quad \left.\frac{\partial \hat{T}_g}{\partial z}\right|_{z=L} = 0 \qquad (20)$$

and the BCs are now time-independent. Let us now define the trial solutions

$$\begin{aligned} \hat{T}_g(z,t) &= \underline{\zeta} \cdot \underline{x_a} \\ T_{\text{cat}}(z,t) &= \underline{\varphi} \cdot \underline{x_b} \end{aligned} \qquad (21)$$

where the number of basis functions for the thermal model are defined as $\tilde{N} = N + 1$, $\underline{\zeta} = [\zeta_0(z), \zeta_1(z), ..., \zeta_N(z)] \in \mathbb{R}^{1\times\tilde{N}}$ and $\underline{\varphi} = [\varphi_0(z), \varphi_1(z), ..., \varphi_N(z)] \in \mathbb{R}^{1\times\tilde{N}}$ are the basis function vectors, $\underline{x_a} = [x_{a,0}(t), x_{a,1}(t), ..., x_{a,N}(t)]^T \in \mathbb{R}^{\tilde{N}\times1}$, $\underline{x_b} = [x_{b,0}(t), x_{b,1}(t), ..., x_{b,N}(t)]^T \in \mathbb{R}^{\tilde{N}\times1}$ are the time-varying coefficients vectors, where the superscript T indicates the transpose operation. The basis functions are defined as

$$\varphi_j(z) = \begin{cases} \sqrt{\dfrac{1}{L}} & j = 0 \\[2mm] \sqrt{\dfrac{2}{L}}\cos\left(\pi j \dfrac{z}{L}\right) & j = 1, ..., N \end{cases} \qquad (22)$$

$$\zeta_j(z) = \sqrt{\frac{2}{L}}\sin\left(\frac{\pi(2j+1)}{2}\frac{z}{L}\right) \quad j = 0, ..., N$$

Figure 4 shows an example of five basis functions. We then substitute Eq. (21) in Eq. (6), and rewrite the equations as Eq. (23), obtaining two quantities which we now define as the residuals r_1 and r_2. The residuals represent the error introduced by substituting the trial solution into the original PDE. Next, we enforce the residuals to be equal to zero by multiplying both equations by the corresponding test functions (ζ for T_g, φ for T_{cat}) and integrating from 0 to L
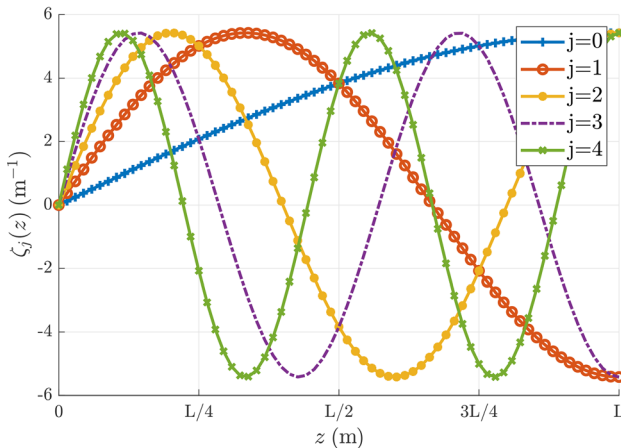
Fig. 4 The first 5 $\zeta_j(z)$ modes, along the TWC axis

$$\begin{aligned} r_1(z,t) &= \frac{\partial(\underline{\zeta}\,\underline{x_a} + f\,T_{\text{exh}})}{\partial t} - \mathcal{D}_1\frac{\partial^2(\underline{\zeta}\,\underline{x_a} + f\,T_{\text{exh}})}{\partial z^2} \\ &\quad + \mathcal{D}_2\dot{m}_{\text{exh}}\frac{\partial(\underline{\zeta}\,\underline{x_a} + f\,T_{\text{exh}})}{\partial z} \\ &\quad - \mathcal{D}_3(\underline{\varphi}\,\underline{x_b} - \underline{\zeta}\,\underline{x_a} - f\,T_{\text{exh}}) = 0 \\ r_2(z,t) &= \frac{\partial(\underline{\varphi}\,\underline{x_b})}{\partial t} - \mathcal{D}_4\frac{\partial^2(\underline{\varphi}\,\underline{x_b})}{\partial z^2} \\ &\quad + \mathcal{D}_5(\underline{\varphi}\,\underline{x_b} - \underline{\zeta}\,\underline{x_a} - f\,T_{\text{exh}}) - \mathcal{D}_6\dot{m}_{\text{exh}} \end{aligned} \qquad (23)$$

$$\int_0^L \underline{\zeta}^T r_1(z,t)\,dz \int_0^L \underline{\varphi}^T r_2(z,t)\,dz \qquad (24)$$

After some basic algebra, the following system of $2\tilde{N}$ ODEs is obtained, where the parameters resulting from the spatial integration of the residuals are defined as

$$\begin{bmatrix} \underline{\dot{x}_a} \\ \underline{\dot{x}_b} \end{bmatrix} = \begin{bmatrix} \mathcal{D}_1\boldsymbol{K_2} - \mathcal{D}_3\boldsymbol{I}_{\tilde{N}} & \mathcal{D}_3\boldsymbol{K_4} \\ \mathcal{D}_5\boldsymbol{K_4}^T & \mathcal{D}_4\boldsymbol{K_5} - \mathcal{D}_5\boldsymbol{I}_{\tilde{N}} \end{bmatrix}\begin{bmatrix} \underline{x_a} \\ \underline{x_b} \end{bmatrix}$$
$$+ \begin{bmatrix} -\boldsymbol{V_3} & -\mathcal{D}_3\boldsymbol{V_3} + \mathcal{D}_1\boldsymbol{V_1} - \mathcal{D}_2\boldsymbol{V_2}\cdot\dot{m}_{\text{exh}} & -\mathcal{D}_2\boldsymbol{K_3}\cdot\underline{x_a} \\ 0 & \mathcal{D}_5\boldsymbol{V_4} & \mathcal{D}_6\boldsymbol{V_5} \end{bmatrix}$$
$$\begin{bmatrix} \dot{T}_{\text{exh}} \\ T_{\text{exh}} \\ \dot{m}_{\text{exh}} \end{bmatrix}$$

$$(25)$$

$$\begin{aligned} \boldsymbol{K_1} &= \int_0^L \underline{\zeta}^T\underline{\zeta}\,dz, & \boldsymbol{K_2} &= \int_0^L \underline{\zeta}^T\frac{\partial^2\underline{\zeta}}{\partial z^2}\,dz \\ \boldsymbol{K_3} &= \int_0^L \underline{\zeta}^T\frac{\partial\underline{\zeta}}{\partial z}\,dz, & \boldsymbol{K_4} &= \int_0^L \underline{\zeta}^T\underline{\varphi}\,dz \\ \boldsymbol{K_5} &= \int_0^L \underline{\varphi}^T\frac{\partial^2\underline{\varphi}}{\partial z^2}\,dz, & \boldsymbol{V_1} &= \int_0^L \underline{\zeta}^T\frac{\partial^2 f}{\partial z^2}\,dz \\ \boldsymbol{V_2} &= \int_0^L \underline{\zeta}^T\frac{\partial f}{\partial z}\,dz, & \boldsymbol{V_3} &= \int_0^L \underline{\zeta}^T f\,dz \\ \boldsymbol{V_4} &= \int_0^L \underline{\varphi}^T f\,dz, & \boldsymbol{V_5} &= \int_0^L \underline{\varphi}^T\,dz \end{aligned} \qquad (26)$$

with $\boldsymbol{K_p} \in \mathbb{R}^{\tilde{N}\times\tilde{N}}$ for $p = 1, ..., 5$ and $\boldsymbol{V_q} \in \mathbb{R}^{\tilde{N}\times1}$ for $q = 1, ..., 5$. The initial conditions $\underline{x_a}(0)$, $\underline{x_b}(0)$ are obtained by substituting $t = 0$ in Eq. (21), and recalling Eqs. (5) and (19). The obtained model is composed of ODEs, and its complexity depends on the number of modes. Compared to other control-oriented thermal models, such as the one presented in Ref. [12], the obtained model is easy-to-tune, it was rigorously developed starting from first laws, and written in a state-space form suitable for state-estimation and control.

4.2 Reduction of the Oxygen Storage Dynamics. Regarding the oxygen storage model, the model reduction using analytical basis, such as the ones used for the thermal model, proved to be inaccurate and led to numerical instabilities. This is possibly due to the stiffness of the input λ_{pre} and the complex nonlinearities governing the storage dynamics (see Ref. [37]). In a future work, a specific implementation of the Galerkin approach for stiff system could be used, such as the one proposed in Ref. [38]. Instead, a solution using numerical bases, obtained through the POD approach, is here presented. The obtained bases are then used to reduce the model order with the Galerkin projection. While the reduction using analytical functions may yield to a nonclosed form integral and thus be impractical for real-time implementation, POD allows to numerically approximate the nonlinear

functions. As anticipated in Sec. 2.2, only the dynamics corresponding to the time evolution of the oxygen storage level ϕ (or equivalently $[Ce_2O_4]$), has been reduced, whereas the three algebraic equations in Eq. (13) are solved in closed form, once ϕ is known. Similar considerations have been done in Ref. [27], for the derivation of a Galerkin-POD-based ROM for Waste Heat Recovery Systems.

4.3 Proper Orthogonal Decomposition. The POD is a numerical method that allows one to generate basis functions to approximate the dynamics of a PDE model using simulation data (see Ref. [39]). This algorithm takes as an input a snapshot matrix $\boldsymbol{S} \in \mathbb{R}^{Z_{\text{stor}} \times \mathcal{T}}$

$$\boldsymbol{S} = [\boldsymbol{S}_1, ..., \boldsymbol{S}_{\mathcal{T}}] \tag{27}$$

where $\mathcal{T}$ is the number of time samples and the matrix rows are spatial discretization points along the TWC z-axis, while the columns are the discretized time instants. The matrix is used to extract the system dynamics and to project them on a lower dimensional subspace: it is therefore critical for the data stored in the matrix to accurately represent the plant behavior, and for the inputs to be as rich in frequencies as possible. A study regarding the aforementioned input-dependent problem is shown in Sec. 5.2. The snapshot matrix is generated simulating the system defined in Sec. 2.2, with $Z_{\text{stor}} = 12$ spatial discretization cells, and a sampling frequency $f_s = 200 \, Hz$. It has been shown in Ref. [18] that no significant improvements are obtained with more cells. Then, a structural value decomposition is performed on the matrix

$$\boldsymbol{S} = \boldsymbol{U}\boldsymbol{\Sigma}\boldsymbol{V}^T \tag{28}$$

where $\boldsymbol{U} \in \mathbb{R}^{Z_{\text{stor}} \times Z_{\text{stor}}}$, $\boldsymbol{V} \in \mathbb{R}^{\mathcal{T} \times \mathcal{T}}$, $\boldsymbol{\Sigma} \in \mathbb{R}^{Z_{\text{stor}} \times \mathcal{T}}$ and

$$
\begin{aligned}
\boldsymbol{U} &= \begin{bmatrix} \boldsymbol{\psi_1} & \cdots & \boldsymbol{\psi_{Z_{\text{stor}}}} \end{bmatrix} \\
\boldsymbol{V} &= \begin{bmatrix} \boldsymbol{v_1} & \cdots & \boldsymbol{v_{\mathcal{T}}} \end{bmatrix} \\
\boldsymbol{\Sigma} &= \begin{bmatrix}
\sigma_1 & 0 & \cdots & 0 & 0 & \cdots & 0 \\
0 & \sigma_2 & 0 & \vdots & \vdots & \vdots & \vdots \\
& & \ddots & & & & \\
\vdots & & & 0 & \vdots & \vdots & \vdots \\
0 & \cdots & 0 & \sigma_{Z_{\text{stor}}} & 0 & \cdots & 0
\end{bmatrix}
\end{aligned} \tag{29}
$$

The matrix Σ stores the σ_i singular values of the snapshot matrix, which are sorted in decreasing order, such that $\sigma_1 > \sigma_2 > \cdots > \sigma_{Z_{\text{stor}}}$, while the spatial-dependent basis functions $\boldsymbol{\psi_1}, ..., \boldsymbol{\psi_{Z_{\text{stor}}}}$ are contained in $\boldsymbol{U}$ (an example of the first five basis functions is shown in Fig. 5). The bases are mutually orthonormal,
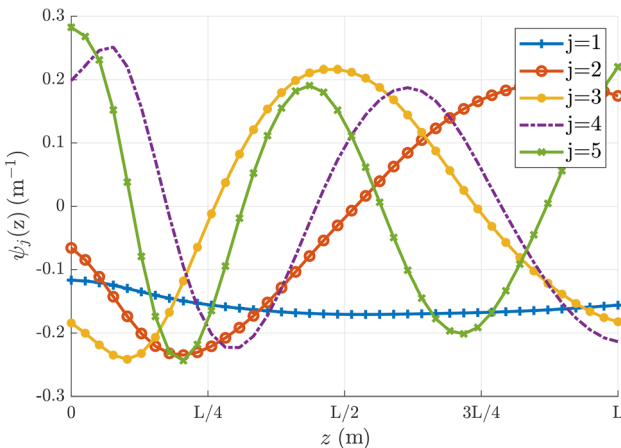
and therefore, their inner product is equal to zero when it is computed between two different bases, and equal to one when it is computed for the same basis, i.e.,

$$\boldsymbol{\psi}_i^T \cdot \boldsymbol{\psi}_j = \begin{cases} 1 & i = j \\ 0 & i \neq j \end{cases} \tag{30}$$

As showed for the thermal model, the number of selected basis functions corresponds to the order of the reduced model. Let us call this number $\tilde{Z} \leq Z_{\text{stor}}$. Given that the singular values are sorted in a decreasing order in Σ, one can note that some of them are predominant and almost completely describe the system dynamics. The heuristic criterion defined for the selection of the number of modes is based on the truncation degree inequality (for instance, as in Ref. [34]) such that $O\tilde{Z} \geq \bar{M}$, with $\bar{M} \in (0, 1]$ and

$$O\tilde{Z} = \frac{\sum_{j=1}^{\tilde{Z}} \sigma_j^2}{\sum_{j=1}^{Z_{\text{stor}}} \sigma_j^2} \tag{31}$$

The results of the procedure applied to the $[Ce_2O_4]$ concentration profile are shown in Fig. 6. As one can observe, seven modes are enough to reconstruct 90% of the original model, for both the FTP and the FUDS cycles and Green catalyst. Finally, once the number of modes to be used for the model-order reduction is selected, the numerical bases are collected in the matrix

$$\underline{\boldsymbol{\psi}} = \begin{bmatrix} \boldsymbol{\psi_1} & \cdots & \boldsymbol{\psi_{\tilde{Z}}} \end{bmatrix} \in \mathbb{R}^{\left(Z_{\text{stor}} \times \tilde{Z}\right)} \tag{32}$$

4.4 Galerkin Projection of the Oxygen Storage Dynamics. Similarly to what was done for the thermal dynamics, the first step consists in selecting a trial solution for the approximated states of the ROM. This consists in multiplying the basis function vector $\underline{\boldsymbol{\psi}}$ (32) by a suitable vector $\underline{\boldsymbol{x_c}} \in \mathbb{R}^{(\tilde{Z} \times 1)}$, whose components are time varying coefficients $[\boldsymbol{x}_{c,1}, ..., \boldsymbol{x}_{c,\tilde{Z}}]^T$

$$[Ce_2O_4](z, t) = \underline{\boldsymbol{\psi}} \cdot \underline{\boldsymbol{x_c}} \tag{33}$$

The residual is then written substituting (33) into the last equation of Eq. (13), following the approach showed in Eq. (4.1)

$$
\begin{aligned}
r_3(z, t) &= \underline{\boldsymbol{\psi}} \cdot \underline{\dot{\boldsymbol{x}}_c} - 2\left(k_1^f \cdot \left(OSC - \underline{\boldsymbol{\psi}} \cdot \underline{\boldsymbol{x_c}}\right)^2 \cdot [\boldsymbol{O_2}] - k_1^b\left(\underline{\boldsymbol{\psi}} \cdot \underline{\boldsymbol{x_c}}\right)^2\right) \\
&+ k_2^f \underline{\boldsymbol{\psi}} \cdot \underline{\boldsymbol{x_c}} \cdot [\boldsymbol{CO}] - -k_2^b \cdot \left(OSC - \underline{\boldsymbol{\psi}} \cdot \underline{\boldsymbol{x_c}}\right) \cdot [\boldsymbol{CO_2}]
\end{aligned} \tag{34}
$$

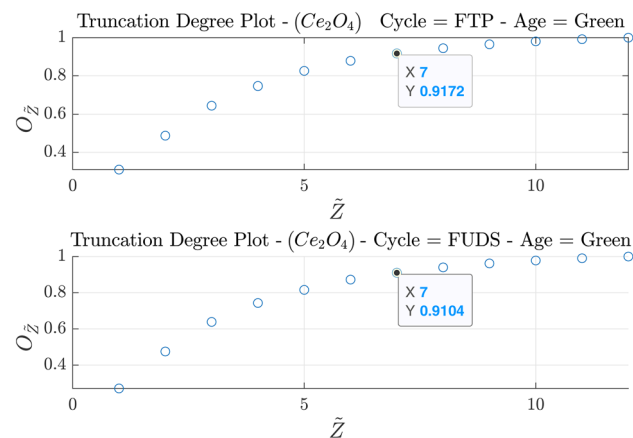Fig. 5 The first 5 $\psi_j(z)$ modes, along the TWC length under the FTP driving cycle

Fig. 6 Truncation degree plot for $[Ce_2O_4]$, for the FTP cycle (upper figure) and the FUDS cycle

Then, both sizes of Eq. (34) are multiplied by the basis function vector $\underline{\psi}$, chosen as a test function. The reduced order model, i.e., the components of the vector $\underline{x}_c$, is obtained by solving the following equation, enforcing the minimization of the error between the reduced model and the original model:

$$\int_0^L \underline{\psi}^T r_3(z,t)\, dz = 0 \qquad (35)$$

Upon using the orthonormality condition (30), the reduced model dynamics is obtained

$$\underline{\dot{x}}_c = \underline{\psi}^T \cdot \left(2\tilde{R}_1 - \tilde{R}_2\right) \qquad (36)$$

where $\tilde{R}_1$ and $\tilde{R}_2$ are obtained substituting Eq. (33) in the reaction rates (9). In this way, the original Z_{stor}-th order discretized model has been reduced to a $\hat{Z}$-th order model. The initial conditions $\underline{x}_c(0)$ for Eq. (36) can be obtained by substituting $t=0$ in Eq. (33) and recalling Eq. (15).

5 Simulation Results

In this section, the ROM performance is compared to the one of the PDE model, for differently aged catalysts and different driving cycles. The RMSE between two time-dependent sampled signals $s_1(k)$ and $s_2(k)$, over N_s time samples is defined as

$$\text{RMSE}(s1, s2) = \sqrt{\frac{\sum_{k=1}^{N_s}\left(s_1(k) - s_2(k)\right)^2}{N_s}} \qquad (37)$$

5.1 Thermal Dynamics. The results of the reduction of the thermal dynamics are compared to the PDE model, discretized using $Z_{therm} = 20$ cells, for different driving cycles and aged catalysts, to verify the effectiveness of the method. A summary of the RMSE between the ROM and the original model is showed in Table 4. Figure 7 shows the performance of the model applied to the Green catalyst, along with the error between the ROM and the original model (the same error metric is repeated in all the plots in this section). As one can note, the ROM prediction correctly reconstructs the original PDE solution, even with a low-order model. The solution obtained with one mode is however inaccurate, and this effectively shows that the thermal dynamics cannot be modeled correctly by assuming a lumped model with one single time-dependent state. The one-state thermal model has been frequently used in the literature for the design of control-oriented models. Figures 8 and 9 show instead the model prediction for the aged catalysts. Let us note that the error is smaller for the latter

Table 4 RMSEs between the predictions of $T_{cat,mid}$ from the PDE and ROM

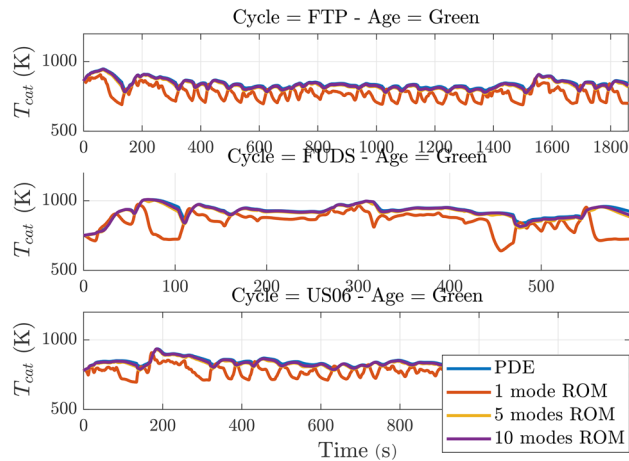|		Catalyst age		
Driving cycle	Number of modes	Green	Midlife	OBD
FTP	1	84.2473 K	61.7595 K	54.8733 K
	5	13.2188 K	7.7448 K	7.9112 K
	10	7.8902 K	4.2562 K	3.4428 K
FUDS	1	110.4783 K	91.8352 K	X
	5	13.5471 K	9.8802 K	X
	10	8.0104 K	5.1521 K	X
US06	1	77.6580 K	X	X
	5	12.3576 K	X	X
	10	7.2444 K	X	X
FHDS	1	X	X	41.5512 K
	5	X	X	5.5718 K
	10	X	X	2.4973 K

Fig. 7 Comparison between predicted $T_{cat,mid}$ from the PDE model and the Galerkin model, for the Green catalyst and the FTP, FUDS, US06 driving cycles (upper, middle, and lower plots)
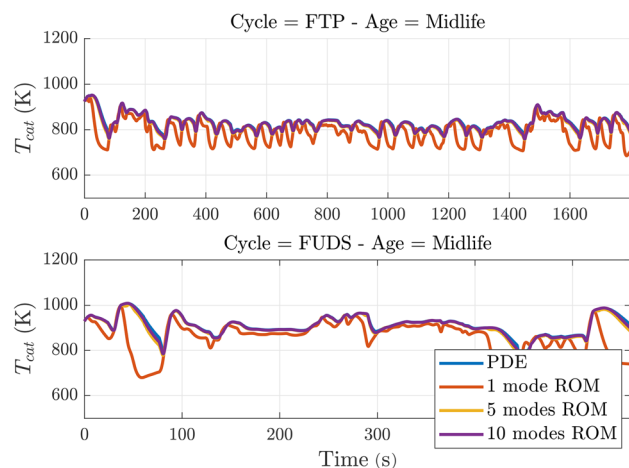

Fig. 8 Comparison between predicted $T_{cat,mid}$ from the PDE model and the Galerkin model, for the Midlife catalyst and the FTP and FUDS driving cycles (upper and lower plots)

with respect to the fresh one, for the same number of modes: this could suggest that the temperature variability with respect to the z-axis is less significant as the catalyst ages, and less modes are enough to correctly reconstruct the thermal dynamics. For the FUDS cycle and the Green catalyst, the computational time for a five mode-ROM is approximately, 9.31 ± 0.36 s.f[1]

5.2 Driving Cycle Characterization. As previously stated, the empirical bases obtained through POD are, in general, inputs dependent. An analysis in the domain of frequencies is performed to characterize the variability and dependence of the number of basis functions for different driving cycles.

First, the model inputs $\dot{m}_{exh}$, λ_{pre}, and T_{exh} are high-pass filtered at 0.01 Hz. This step is necessary in order to detrend the variables and capture only the information regarding the frequency variations.

Then, the power spectral density (PSD) is computed for the different signals, and the obtained points are normalized with respect to the maximum power in the frequency spectrum: in this way different cycles can be compared. From Fig. 10, one can note that the frequency content for $\dot{m}_{exh}$ is similar for different driving cycles. This means that the dynamics are excited in similar ways

---

[1]This is obtained from simulating the ROM 20 times on a 4 GHz Intel i7 processor, 8 GB RAM PC using MATLAB 2019a.

in the three different cycles, and the POD should yield similar results in terms of basis functions. Similar considerations can be done for T_{exh}, with the only difference being the richer low-frequency content. The same can be observed for λ_{pre} (Fig. 11) even if for the FUDS cycle a richer low-frequency content can be noted. Figures 12–15 show the results of the analysis for the aged catalyst, where similar considerations can be drawn.
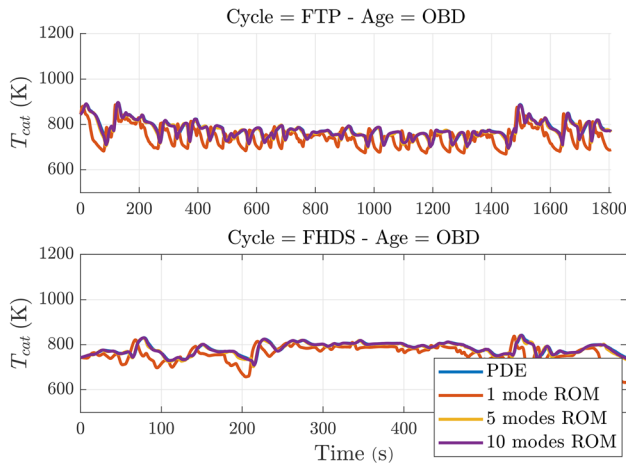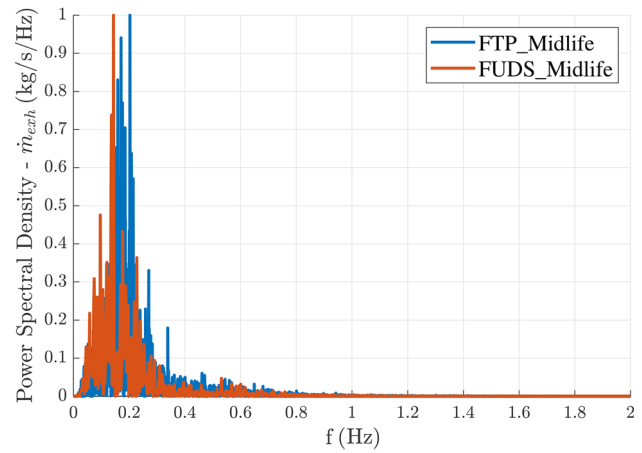

Fig. 9 Comparison between predicted $T_{cat,mid}$ from the PDE model and the Galerkin model, for the OBD catalyst and the FTP and FHDS driving cycles (upper and lower plots)

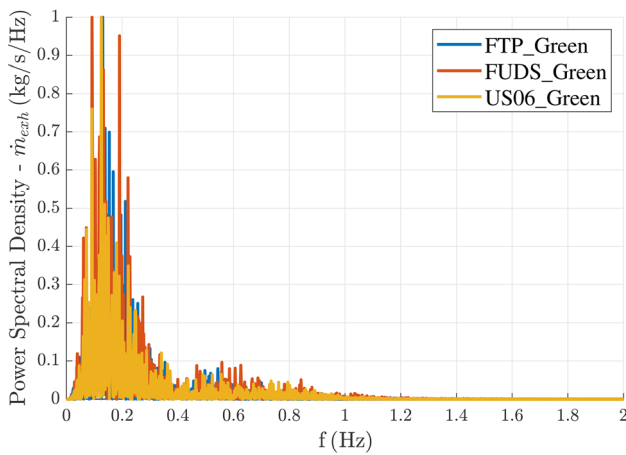**Fig. 10 PSD for $\dot{m}_{exh}$, for the Green catalyst and the FTP, FUDS and US06 driving cycles**

Fig. 11 PSD for λ_{pre}, for the Green catalyst and the FTP, FUDS and US06 driving cycles

Fig. 12 PSD for $\dot{m}_{exh}$, for the Midlife catalyst and the FTP and FUDS driving cycles

Fig. 13 PSD for λ_{pre}, for the Midlife catalyst and the FTP and FUDS driving cycles

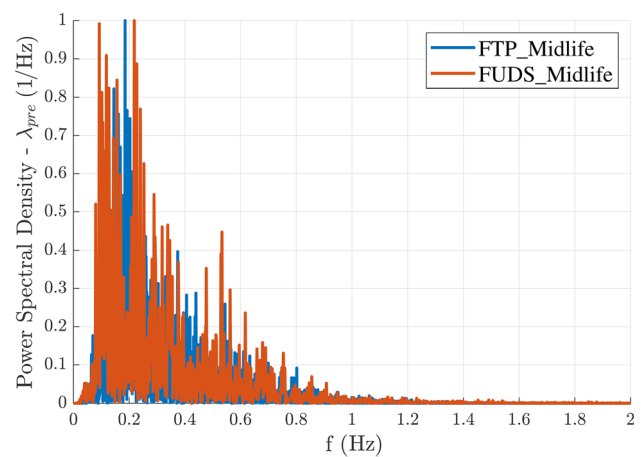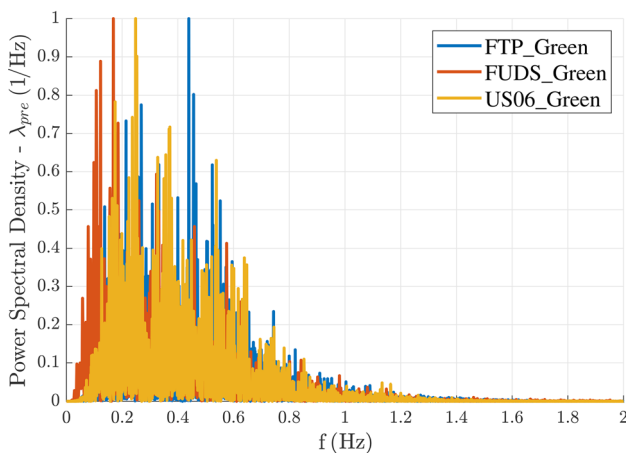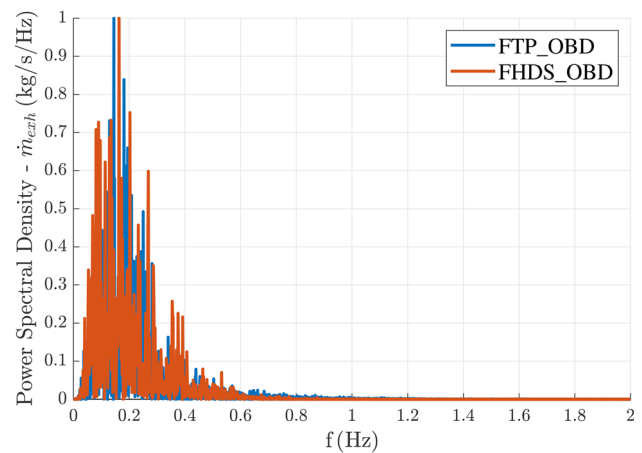**Fig. 14 PSD for $\dot{m}_{exh}$, for the OBD catalyst and the FTP and FHDS driving cycles**
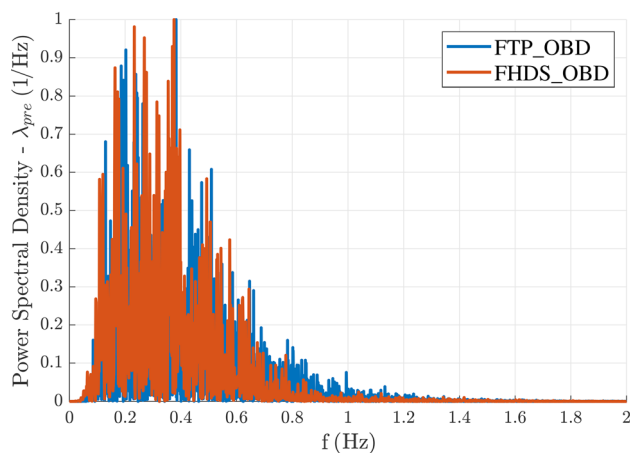
Fig. 15 PSD for λ_{pre}, for the OBD catalyst and the FTP and FHDS driving cycles

5.3 Oxygen Storage Dynamics.
The results of the reduction of the oxygen storage dynamics are compared to the PDE model, for different driving cycles and catalyst aging processes, to verify the effectiveness of the method.

In the following results, the basis functions have been obtained from the FTP cycle. The prediction of ϕ for the Green catalyst and the FTP and FUDS driving cycles is shown in Fig. 16. As one can note, the overall prediction with six and eight modes is good and the PDE model results are well approximated by the ROM. The one mode simulations were also performed, corresponding to a one-state ROM, and results are shown in Fig. 16 as well. Predictions obtained using one-state model do not provide a reliable estimate of the oxygen storage level, as it was also observed for the thermal dynamics. It is worth mentioning that that single-state control-oriented models have been widely used in previous studies [12,23].

Figures 17 and 18 show the ROM versus PDE comparison for the midlife and OBD catalysts. The RMSEs between the reduced model prediction and the PDE prediction are showed in Table 5.
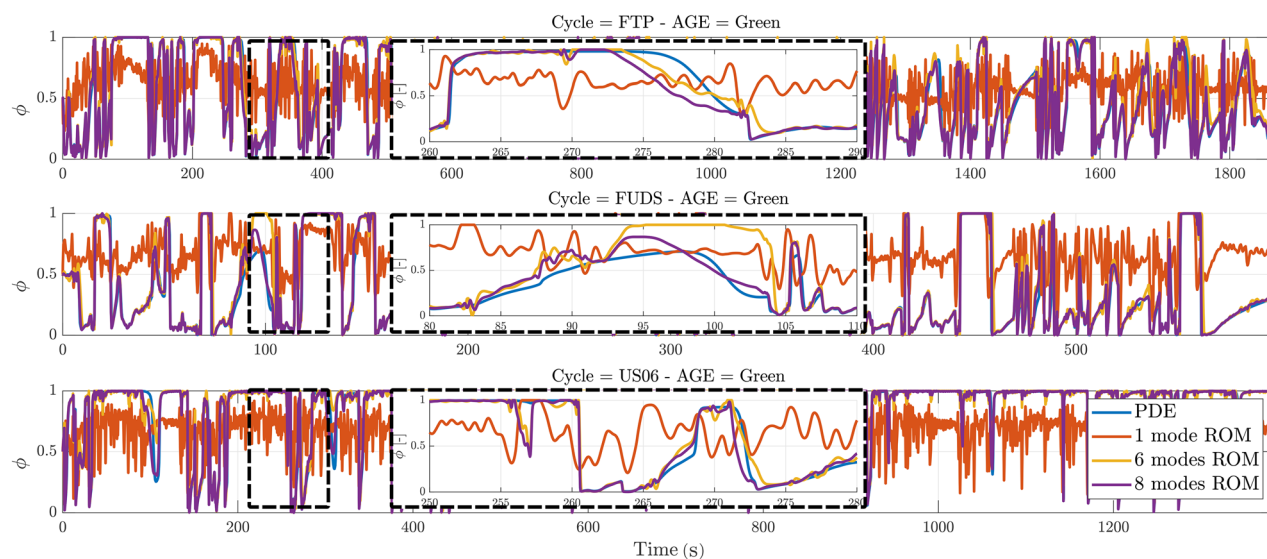

Fig. 16 Comparison between predicted ϕ from the PDE model and the POD-Galerkin model, for the Green catalyst and the FTP, FUDS, US06 driving cycles (upper, middle, and lower plots)
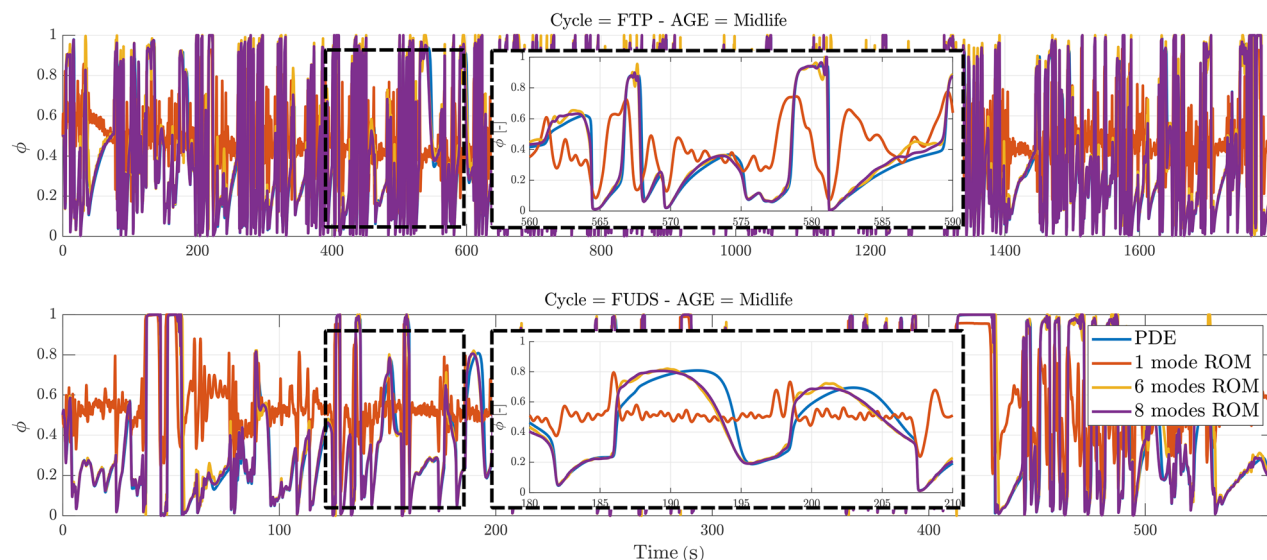

Fig. 17 Comparison between predicted ϕ from the PDE model and the POD-Galerkin model, for the midlife catalyst and the FTP and FUDS driving cycles (upper and lower plots)
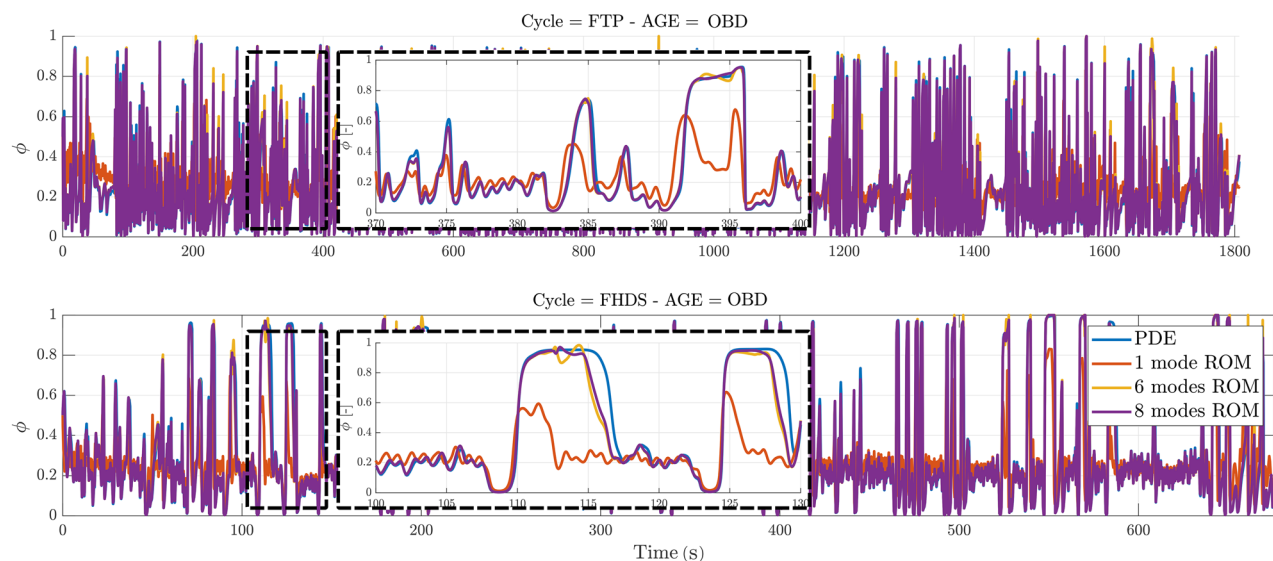
Fig. 18 Comparison between predicted ϕ from the PDE model and the POD-Galerkin model, for the OBD catalyst and the FTP and FHDS driving cycles (upper and lower plots)

Table 5 RMSEs between the predictions of ϕ from the PDE and ROM

		Catalyst age		
Driving cycle	Number of modes	Green	Midlife	OBD
FTP	1	0.3329	0.3318	0.1881
	6	0.0657	0.1024	0.0489
	8	0.0162	0.0411	0.0045
FUDS	1	0.4729	0.3369	X
	6	0.1024	0.0726	X
	8	0.0349	0.0169	X
US06	1	0.3462	X	X
	6	0.0582	X	X
	8	0.0139	X	X
FHDS	1	X	X	0.1887
	6	X	X	0.0173
	8	X	X	0.0060

Similarly to the thermal dynamics, the prediction error is smaller for the aged catalysts, for the same number of selected modes (see Table 5). This can be explained resorting to the fact that aging yield less variability along the z-axis, therefore less modes are required to approximate the PDE dynamics correctly. These results allow to design a ROM by just looking at the performance for a fresh catalyst. For the FUDS cycle and the Green catalyst, the computational time for a six-mode ROM is approximately $2.16 \pm 0.27 \, s.$[2] Finally, one should note that even if the set of basis functions was extracted through POD from the Green catalyst, their effectiveness is retained for different driving cycles and for differently aged catalysts. This shows that this application does not suffer from the input-dependence of the POD algorithm.

6 Conclusion

In this paper, a reduced-order model for the thermal and oxygen storage dynamics of a TWC was developed, starting from a physics-based PDE model. The physics-based model was partially borrowed from previous research, and a few terms have been added to the thermal dynamics of the catalyst in order to obtain a more general formulation. The resulting model showed to be effective in reproducing the behavior of the original model, and

has been exhaustively tested against real data coming from three differently aged catalysts and various driving cycles. The developed model can be used to reduce the computational burden on the ECU, in the framework of an emission minimization control strategy. The effectiveness of the methodology proposed in this study allows the design of a control-oriented model whose accuracy is directly quantifiable with respect to the real behavior of the system. Moreover, such a control-oriented model has been showed to have consistent performance throughout the device life.

Nomenclature

A_{cs} = TWC cross-sectional area (m^2)
A_{geo} = TWC specific geometric area (m^{-1})
A_i = pre-exponential factor for reaction i
$c_{p,g}$ = exhaust gas specific heat (J kg^{-1} K^{-1})
$c_{p,s}$ = TWC solid-phase specific heat (J kg^{-1} K^{-1})
c_0 = total exhaust gas concentration (N mol^{-2} J^{-1})
E_i = activation energy for reaction i (J mol^{-1})
h = convective heat transfer coefficient (W m^{-2} K^{-1})
i = reaction index
j = basis function index
k = time sample index
K_{reac} = proportional constant for the heat produced by reactions (J kg^{-1} m^{-3})
k_i^f = forward reaction rate for reaction i
k_i^b = backward reaction rate for reaction i
l = oxygen storage model spatial discretization index
L = catalyst length (m)
M_{exh} = average molar mass of the exhaust gas (kg mol^{-1})
$\dot{m}_{\mathrm{exh}}$ = mass rate of the exhaust gas at the TWC inlet (kg s^{-1})
N = number of basis functions for the reduced order thermal model
OSC = oxygen storage capacity (mol m^{-3})
P = ambient pressure (N m^{-2})

---

[2]This is obtained from simulating the ROM 20 times on a 4 GHz Intel i7 processor, 8 GB RAM PC using MATLAB 2019a.

R = universal gas constant (J mol^{-1} K^{-1})
R_i = reaction rate for reaction i (mol m^{-3}s^{-1})
t = time (s)
T_{cat} = TWC solid-phase temperature (K)
T_g = TWC gas-phase temperature (K)
T_{exh} = temperature of the exhaust gas at the TWC inlet (K)
$T_{light-off}$ = TWC light-off temperature (K)
TWC = three-way catalyst
u = flow speed (m s^{-1})
US06 = US06 test protocol
$[X]$ = concentration of species X (mol m^{-3})
z = coordinate along catalyst length (m)
$\tilde{Z}$ = number of basis functions for the reduced order oxygen storage model
Z_{stor} = number of discretization cells for the PDE oxygen storage model
Z_{therm} = number of discretization cells for the PDE thermal model
ΔG_i = Gibbs free energy variation for reaction i (J)
Δz_{therm} = discretization step for the thermal model (m)
Δz_{stor} = discretization step for the oxygen storage model (m)
ϵ = TWC open cross-sectional area
λ = normalized air–fuel ratio
λ_g = exhaust gas conductivity (W m^{-1} K^{-1})
λ_s = TWC solid-phase conductivity (W m^{-1} K^{-1})
ρ_g = exhaust gas density (kg m^{-3})
ρ_s = TWC solid-phase density (kg m^{-3})
φ_j = j-th basis function for the catalyst temperature, in the reduced order thermal model (m^{-1})
ζ_j = j-th basis function for the exhaust gas temperature, in the reduced order thermal model (m^{-1})
ψ_j = j-th basis function for the reduced order oxygen storage model (m^{-1})
ϕ = normalized oxygen storage level

References

[1] U.S. EPA, 2011, "Report on the 2011 U.S. Environmental Protection Agency (EPA) Decontamination Research and Development Conference," U.S. Environmental Protection Agency, Washington, DC, EPA/600/R/12/557, accessed Sept. 25, 2020, http://yosemite.epa.gov/opa/admpress.nsf

[2] Bloomberg New Energy Finance, 2016, "Electric Vehicles to Be 35% of Global New Car Sales by 2040," Bloomberg New Energy Finance, accessed Sept. 29, 2020, https://www.prnewswire.com/news-releases/electric-vehicles-to-be-35-of-global-new-car-sales-by-2040-300225689.html

[3] Delphi Technologies, 2020, "Worldwide Emission Standards, Passengers Cars and Light Duty Vehicles," Delphi Technologies, accessed Sept. 29, 2020, https://www.delphi.com/innovations/emissions-standards-booklets

[4] United States Environmental Protection Agency, 2013, "Tier 3 Motor Vehicle Emission and Fuel Standards," United States Environmental Protection Agency, accessed Sept. 29, 2020, https://www.epa.gov/regulations-emissions-vehicles-and-engines/final-rule-control-air-pollution-motor-vehicles-tier-3

[5] Tripathy, S., Sahoo, S., and Srivastava, D. K., 2017, *Gasoline Direct Injection—Challenges*, Springer, Singapore, pp. 367–379.

[6] Arunachalam, H., Pozzato, G., Hoffman, M. A., and Onori, S., 2017, "Modeling the Thermal Dynamics Inside a Ceria-Coated Gasoline Particulate Filter," First Annual IEEE Conference on Control Technology and Applications, CCTA 2017, Kohala Coast, HI, Aug. 27–30, pp. 99–105.

[7] Faiz, A., Weaver, C., and Walsh, M., 1996, "*Air Pollution From Motor Vehicles: Standards and Technologies for Controlling Emissions*," World Bank Publications, Washington, DC.

[8] Abd-Alla, G., 2002, "Using Exhaust Gas Recirculation in Internal Combustion Engines: A Review," Energy Convers. Manage., **43**(8), pp. 1027–1042.

[9] Arunachalam, A., Pozzato, G., Hoffman, M., and Onori, S., 2020, "Modeling the Thermal and Soot Oxidation Dynamics Inside a Ceria-Coated Gasoline Particulate Filter," Control Eng. Pract., **94**, p. 104199.

[10] Duprey, R., 1968, "Compilation of Air Pollutant Emission Factors," U.S. Department of Health, Education, and Welfare, Washington, DC, Report No. 999-AP-42.

[11] Garrett, 2020, Garrett Advancing Motion, accessed Sept. 29, 2020, http://www.turbobygarrett.com/turbobygarrett/airfuel_ratio_tuning_rich_vs_lean

[12] Brandt, E., Wang, Y., and Grizzle, J., 2000, "Dynamic Modeling of a Three-Way Catalyst for si Engine Exhaust Emission Control," IEEE Trans. Control Syst. Technol., pp. 767–776.

[13] Depcik, C., and Assanis, D., 2005, "One-Dimensional Automotive Catalyst Modeling," Prog. Energy Combust. Sci., **31**(4), pp. 308–369.

[14] Shamim, T., Shen, H., Sengupta, S., Son, S., and Adamczyk, A., 2002, "A Comprehensive Model to Predict Three-Way Catalytic Converter Performance," ASME J. Eng. Gas Turbines Power, **124**(2), pp. 421–428.

[15] Montenegro, G., and Onorati, A., 2009, "1-d Thermo-Fluid Dynamic Modeling of Reacting Flows Inside Three-Way Catalytic Converters," SAE Technical Paper No. 2009-01-1510.

[16] Brinkmeier, C., 2006, "Automotive Three Way Exhaust Aftertreatment Under Transient Conditions: Measurements, Modeling and Simulation," Ph.D. thesis, Universität Stuttgart, Stuttgart, Germany.

[17] Auckenthaler, T., 2005, "Modelling and Control of Three-Way Catalytic Converters," Ph.D. dissertation, Swiss Federal Institute of Technology, ETH Zurich, Germany.

[18] Sabatini, S., Gelmini, S., Hoffman, M. A., and Onori, S., 2017, "Design and Experimental Validation of a Physics-Based Oxygen Storage—Thermal Model for Three Way Catalyst Including Aging," Control Eng. Pract., **68**, pp. 89–101.

[19] Santillo, M., Magner, S., Uhrich, M., and Jankovic, M., 2015, "Towards ECU-Executable Control-Oriented Models of a Three-Way Catalytic Converter," ASME Paper No. DSCC2015-9653.

[20] Utz, T., Fleck, C., Frauhammer, J., Seiler-Thull, D., and Kugi, A., 2014, "Extended Kalman Filter and Adaptive Backstepping for Mean Temperature Control of a Three-Way Catalytic Converter," Int. J. Robust Nonlinear Control, **24**(18), pp. 3437–3453.

[21] Simon, A., Nelson-Gruel, D., Onori, S., Charlet, A., Jaine, T., Colin, G., Nouillant, C., and Chamaillard, Y., 2019, "An Observer Looks at the Temperature in the 3wcc," **52**(5), pp. 531–537.

[22] Bekiaris-Liberis, N. M., Jankovic, M., and Krstic, 2012, "PDE-Based Analysis and Control of the Oxygen Storage Level in Three-Way Catalytic Converters," IEEE 51st IEEE Conference on Decision and Control, Maui, HI, Dec. 10–13, pp. 3759–3764

[23] Soumelidis, M., Stobart, R., and Jackson, R., 2014, "A Nonlinear Dynamic Model for Three-Way Catalyst Control and Diagnosis," SAE Technical Paper No. 2004-01-1831.

[24] Tomforde, M., Drewelow, W., Duenow, P., Lampe, B., and Schutalbers, M., 2013, "A Post-Catalyst Control Strategy Based on Oxygen Storage Dynamics," SAE Technical Paper No. 2013-01-0352.

[25] Stabile, G., Hijazi, S., Mola, A., Lorenzi, S., and Rozza, G., 2017, "Pod-Galerkin Reduced Order Methods for Cfd Using Finite Volume Discretisation: Vortex Shedding Around a Circular Cylinder," Commun. Appl. Ind. Math., **8**(1), pp. 210–236.

[26] Marquez, A., Oviedo, J. E., and Odloak, D., 2013, "Model Reduction Using Proper Orthogonal Decomposition and Predictive Control of Distributed Reactor System," J. Control Sci. Eng., **2013**, pp. 1–19.

[27] Xu, B., Yebi, A., Hoffman, M., and Onori, S., 2020, "A Rigorous Model Order Reduction Framework for Waste Heat Recovery Systems Based on Proper Orthogonal Decomposition and Galerkin Projection," IEEE Trans. Control Syst. Technol., **28**(2), pp. 635–643.

[28] Godi, R., and Onori, S., 2017, "Reduced Order Model Design for Three Way Catalytic Converter Temperature Dynamics," IEEE Conference on Control Technology and Applications (CCTA), Kohala Coast, Hawai'i, August 27–30, pp. 886–891.

[29] Zhu, Z., Midlam-Mohler, S., and Canova, M., 2019, "Development of Physics-Based Three-Way Catalytic Converter Model for Real-Time Distributed Temperature Prediction Using Proper Orthogonal Decomposition and Collocation," Int. J. Engine Res., pp. 1–17.

[30] Kiwitz, P., Onder, C., and Guzzella, L., 2012, "Control-Oriented Modeling of a Three-Way Catalytic Converter With Observation of the Relative Oxygen Level Profile," J. Process Control, **22**(6), pp. 984–994.

[31] Sabatini, S., Kil, I., Dekar, J., Hamilton, T., Wuttke, J., Smith, M. A., Hoffman, M. A., and Onori, S., 2015, "A New Semi-Empirical Temperature Model for the Three Way Catalytic Converter". IFAC Workshop on Engine and Powertrain Control," Simul. Model. E-COSM, **48**(15), pp. 434–440.

[32] Skeel, R., and Berzins, M., 1990, "A Method for the Spatial Discretization of Parabolic Equations in One Space Variable," SIAM J. Sci. Stat. Comput., **11**(1), pp. 1–32.

[33] Guzzella, L., and Onder, C., 2009, *Introduction to Modeling and Control of Internal Combustion Engine Systems*, Springer Science & Business Media, Berlin.

[34] Ebbesen, S., Kiwitz, P., and Guzzella, L., 2012, "A Generic Particle Swarm Optimization Matlab Function," 2012 Am. Control Conf. (ACC), pp. 1519–1524.

[35] Kennedy, J., and Eberhart, R., 1995, "Particle Swarm Optimization," Proceedings of ICNN'95 - International Conference on Neural Networks, Vol. 4, Perth, WA, Australia, Nov. 27 to Dec. 1, pp. 1942–1948.

[36] Giuliano, M., Ricchiardi, G., Damin, A., Sgroi, M., Nicol, G., and Parussa, F., 2020, "Thermal Ageing Effects in a Commercial Three-Way Catalyst: Physical Characterization of Washcoat and Active Metal Evolution," Int. J. Automot. Technol., **21**(2), pp. 329–337.

[37] Carlberg, K., Barone, M., and Antil, H., 2017, "Galerkin v. least-Squares Petrov-Galerkin Projection in Nonlinear Model Reduction," J. Comput. Phys., **330**, pp. 693–734.

[38] Logg, A., 2004, "Multi-Adaptive Time Integration," Appl. Numer. Math., **48**(3–4), pp. 339–354.

[39] Pinnau, R., 2008, *Model Reduction via Proper Orthogonal Decomposition*, Vol. 13, Springer, Berlin/Heidelberg, pp. 95–109.